

Research Article

Small Signals' Study of Thermal Induced Current in Nanoscale SOI Sensor

Yaakov Mandelbaum,¹ Ilan Gadasi,¹ Avraham Chelly,² Zeev Zalevsky,³ and Avi Karsenty¹

¹Lev Academic Center, Faculty of Engineering, Department of Applied Physics/Electro-Optics Engineering, 9116001 Jerusalem, Israel

²Semiconductor Devices Laboratory, Faculty of Engineering, Bar-Ilan University, 52900 Ramat Gan, Israel

³Department of Electro-Optics, Faculty of Engineering, Bar-Ilan University, 52900 Ramat Gan, Israel

Correspondence should be addressed to Avi Karsenty; karsenty@jct.ac.il

Received 5 September 2017; Accepted 16 October 2017; Published 5 November 2017

Academic Editor: Lucio Pancheri

Copyright © 2017 Yaakov Mandelbaum et al. This is an open access article distributed under the Creative Commons Attribution License, which permits unrestricted use, distribution, and reproduction in any medium, provided the original work is properly cited.

A new nanoscale SOI dual-mode modulator is investigated as a function of optical and thermal activation modes. In order to accurately characterize the device specifications towards its future integration in microelectronics circuitry, current time variations are studied and compared for “large signal” constant temperature changes, as well as for “small signal” fluctuating temperature sources. An equivalent circuit model is presented to define the parameters which are assessed by numerical simulation. Assuring that the thermal response is fast enough, the device can be operated as a modulator via thermal stimulation or, on the other hand, can be used as thermal sensor/imager. We present here the design, simulation, and model of the next generation which seems capable of speeding up the processing capabilities. This novel device can serve as a building block towards the development of optical/thermal data processing while breaking through the way to all optic processors based on silicon chips that are fabricated via typical microelectronics fabrication process.

1. Introduction

Since the nanotechnology is rapidly progressing, the need for smart and complex devices becomes very high. Controlling the current activities using photo- and/or thermoactivation mode may be useful for optoelectronics applications as well as bolometric control systems in electronic circuitry. Nanoscale silicon-based optoelectronic devices are under investigation and development for more than two decades.

The interest for coupling both electronic and optic behaviors is very high, since such devices can be integrated in a smooth way inside the circuits of the existing microelectronics industry [1–3]. The constantly growing use of real time computing generates constant urge for much faster processors than those which are currently available in the market. Correspondingly there is an accelerated development of new optics communication related applications and components. The effort to combine those two trends leads to the generation of new optoelectronic nanodevices. Such hybrid devices may allow high operation speed, reduced cross talk and other

noises, and low operation power and obviate the need for the existing electrooptical converters.

In this perspective, several types of hybrid devices are developed. Part of them are light emitting devices when the activation is electrical, for example, electroluminescence based devices [4–6], and part of them are receptor devices [7–10] such as the SOIPAM (Silicon-On-Insulator Photo-Activated Modulator) nanoscale improved device, in which the modulation control command is optic, as previously reported [11–13]. Additional investigations and simulations brought some breakthrough in this modulator, when it appears that thermal activation which could be related to the absorption of RF radiation, for instance, enables turning the device into a thermal sensor. Indeed, several types of material and size [14, 15] of silicon-based/CMOS nanoscale thermal sensors become much more desirable for integration in microelectronics circuitry [16–28]. So, in our previous work [29] we presented a dual-mode device: Silicon-On-Insulator Photo-Activated Modulator (SOIPAM) combined with Silicon-On-Insulator Thermo-Activated Modulator (SOITAM). The analysis focused on

large signals of the SOITAM photodetector's thermal properties. We extend here this analysis to small signals in the RF frequency domain [25], for example, considering both an analytic model and numerical simulations of the device. We will see a demonstration of a feature of the nanoscale device, due to its small dimensions thermal equilibration being extremely rapid. The large signal simulation demonstrated that response times are very small. The small signal simulation similarly demonstrates that the thermal phase lag is insignificant up to frequencies of 500 MHz or 1 GHz, which are not encountered in practice in thermal settings. Thus, though in principle the system acts as a low pass filter, as will be explained, the simulation demonstrates that attenuation is not encountered until frequencies are so high, as to be irrelevant for practical purposes.

2. Device Structure

Starting from a SOI material, our device is similar to an inverted MOSFET transistor but the modulation of the drain current is achieved via a modulated illumination of the substrate rather than a classic gate voltage modulation. The channel consists of a 30 nm thick n-type silicon channel contacted to source and drain terminals and insulated from the substrate by a 30 nm thick buried oxide layer. A negative gate potential V_{GS} is applied to the bottom side of the p-type silicon substrate such that a negatively charged depletion layer appears under the buried oxide layer. Consequently, a positively charged depletion layer is generated inside the n-type channel upon the buried oxide. The channel thickness and the doping of the p and n regions are designed so the channel is still partially depleted in such conditions.

In dark conditions, an inversion layer of electrons will build up under the buried oxide by thermal generation and enlarge the positive depletion layer in the n-type region, eventually closing the channel. A solution to this problem consists of applying a rapid modulation of the gate potential V_{GS} to keep p-type area in deep depletion. By synchronously illuminating the p-type area through a 10 μm depth V-groove (etched deep inside the substrate and close to the channel), free photo-generated electrons concentration can be significantly increased until the inversion state is reached. As a result, the n-type channel will be fully depleted so the drain current decreases significantly. V-groove receiving area is presented in Figure 1 and complex mesh is presented in Figure 2. The device specifications and dimensions are summarized in Table 1.

3. Response Time Results

In previous work [29] a large signal analysis was made of the SOITAM photodetector's thermal properties. We continue this analysis here considering both an analytic model and numerical simulations. We start with an investigation of response times to a changing temperature. The thermal behavior is strongly parallel to the electrical behavior of a capacitor and resistor in series; it is natural then to consider the two cases of a large and constant temperature change

TABLE 1: SOITAM nanoscale device 3rd generation.

Parameters	Values
Substrate width	250 nm
Substrate length	65 nm
Substrate height	100 nm
V-groove length	100 nm
V-groove height	70 nm
Box thickness	30 nm
Channel thickness t	30 nm
Channel length L	45 nm
Channel width W	22 nm

and of a small fluctuating temperature variation. In the first instance we will find a recovery time, just as for a discharging capacitor, and in the second a phase lag and complex impedance, like that of a capacitor connected to an AC source.

Heat propagation is simulated by numerical computation of the solution to the heat equation in the two-dimensional cross section of the device depicted in Figure 3. The Finite Elements Method (FEM) was implemented using the Comsol software and the temperature distribution $T(\vec{r}, t)$. The boundary conditions used were the following: at the bottom of the device a Dirichlet boundary condition corresponding to the time-dependent external temperature source is implemented. The remaining three sides are taken to be thermally isolated; that is, a state of no heat flux is imposed:

$$\vec{J}_{\text{th}} \cdot \vec{n} = 0, \quad (1)$$

where

$$\vec{J}_{\text{th}} \equiv -k\vec{\nabla}T \quad (2)$$

is the heat current density. This dictates the Neumann boundary condition:

$$\frac{dT}{dn} = \vec{\nabla}T \cdot \vec{n} = 0. \quad (3)$$

At the internal material interfaces, continuity was imposed on the temperature and on the heat current density.

3.1. "Large Signal" Constant Temperature Changes. Using the explicit temperature dependence of the current [29], we can next model the time variation of the current. In particular we may model the time response to the temperature perturbation in the simulation. There the temperature of the boundary is suddenly raised or lowered by a large amplitude and then held fixed until equilibration. Insofar as the channel is located at the far end of the device, it samples the temperature at its location across the length of the device from the location of the temperature disturbance. We may thus use a lumped model for the thermal properties, the heat capacitance and heat conductivity, rather than a detailed distributed model. Thus we need only to consider the total lumped thermal properties, the total heat capacitance and heat conductivity. This allows

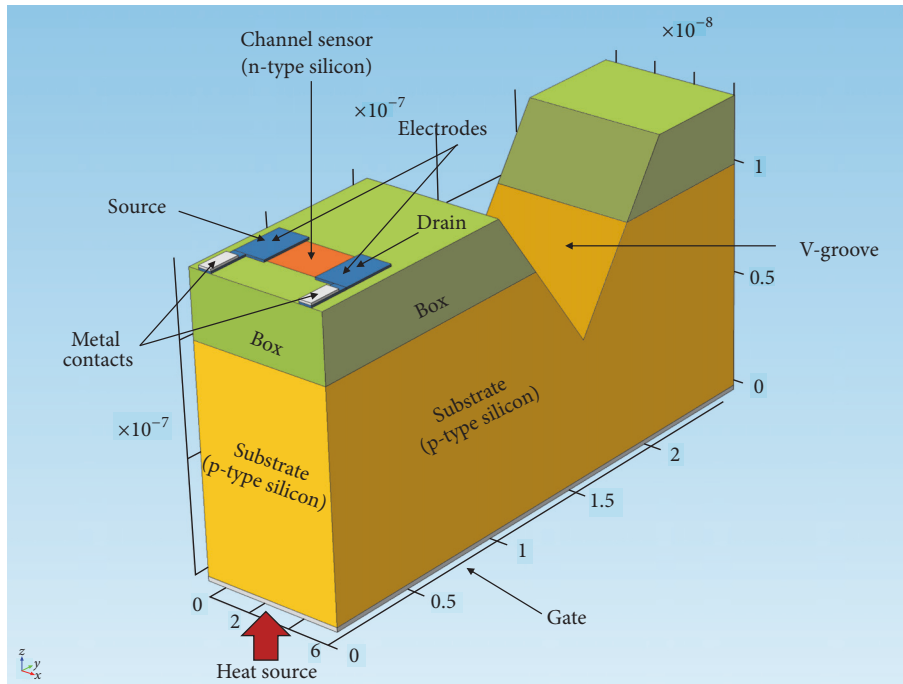


FIGURE 1: COMSOL 3D simulated view of the SOITAM device.

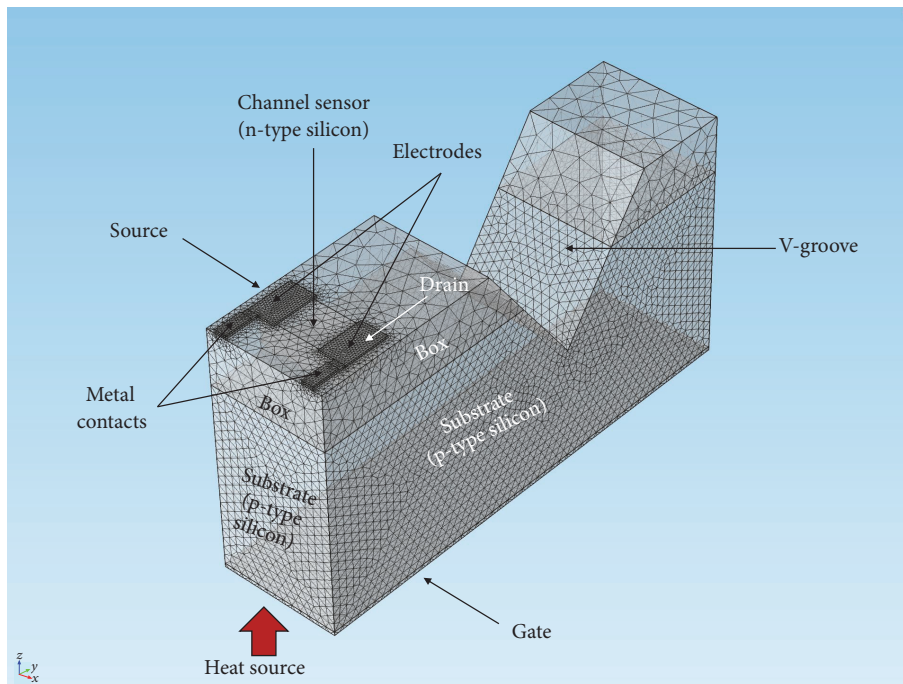


FIGURE 2: COMSOL 3D simulated view of the SOITAM device complex mesh.

the use of an effective description in terms of an equivalent electrical circuit. The equivalent system is described by the discharge of a capacitor; the heat conductance g_{th} plays the role of the electrical conductance $g = 1/R$, the heat capacity C_{th} plays the role of the capacitance C , and the temperature difference ΔT between the two ends of the device supplies the voltage drop ΔV .

The voltage across a discharging capacitor is described by a time-decaying exponential. In a similar fashion, the solution to the thermal problem, the temperature difference, decays exponentially in time with time constant RC . The channel end, isolated on one side, equalizes its temperature to the temperature of the opposite side. Since the temperature dependence of the current was nearly linear, the current will

also display an exponential (-like) decay/recovery. Regardless of the functional form of the current-temperature variation, the decay/recovery time will be given by RC. The parameters required are the specific heat capacity C_{th} and the thermal conductivity k of the substrates and the oxide, together with their respective volumes. Both of the first two parameters, in particular the conductivity, are presumably affected by the presence of the dopants. Figure 3 shows the 30 K large pulse applied at the bottom of the device structure.

3.2. “Small Signal” Fluctuating Temperature Sources. The same equivalent circuit will also model the response to small signals, that is, periodic, time varying temperature perturbations. The equivalent electrical circuit, an RC circuit with AC voltage source, behaves as a low pass filter; hence the amplitude of the temperature drop decreases at high frequencies.

It should be emphasized that the equivalent circuit directly models the temperature response of the channel end. However, for temperature variations of sufficiently small amplitude, the response of the current in the channel will be essentially linear. Even for relatively large amplitudes, however, the near-linearity of the temperature dependence found in [29] means that the equivalent circuit description will be accurate, and the response of the channel current ought to show little distortion of the input temperature signal. The equivalent circuit model is thus expected to be useful for the small signal analysis as well. We note here that thermal back reaction of the current in the channel via Ohmic heating was not taken into account in this analysis. A fully coupled analysis will be presented in a later study.

3.3. RC Equivalent Circuit Model. We present here the mathematical model for the thermal dynamics followed by a description of the equivalent circuit. In the small signal analysis, the device is activated with an initial background temperature T_B applied uniformly. A time-dependent perturbation $\Delta T(t)$ is then applied at the lower boundary so that the temperature there is

$$T_L = T_B + \Delta T(t). \quad (4)$$

In the large signal analysis

$$\Delta T(t) = \Delta T_0 H(t), \quad (5)$$

where $H(t)$ is the Heaviside step function, and ΔT_0 is the amplitude. The latter is assumed to be relatively large, for example, between 10% and 50% of the T_B value. In the small signal analysis,

$$\Delta T(t) = \Delta T_0 \sin \omega t \quad (6)$$

for an angular frequency ω . The amplitude is assumed to be small; that is, $\Delta T_0/T_B \lesssim 2\%$.

We are interested in the time response behavior of the temperature T_U at the far (upper) boundary end of the substrate where the channel is located. For simplicity, we model the device bulk between the boundaries using two lumped

elements, a conductive element with (total) heat conductance, g_{th} , and a capacitive element, with (total) heat capacity C_{th} . A precise calculation must consider that the heat capacitance is distributed throughout the conducting medium. The lumped model considers the capacitive elements as being located at a point, sharing a common effective heat capacitance, and displaying a single representative temperature T_U .

The capacitive elements thus display a distribution of temperatures between T_U and T_B , the temperature at the upper boundary, and the initial background temperature, respectively. The representative temperature is a gauge of the total thermal energy absorbed throughout the bulk; the simplest choice is then the temperature at the far, upper end, where the channel is located. Investigating the results of the simulation, we will determine an effective value for the product of the heat resistance, R_{th} , and the heat capacity C_{th} relative to this choice.

Calibrating with reference to the DC background component we may write

$$\Delta T \equiv T_L - T_B = T_L - T_U + T_U - T_B \equiv \Delta T_g + \Delta T_{C_{th}}. \quad (7)$$

The first term, which describes the temperature difference between the ends of the device, is modeled by the temperature drop on the conductive element, ΔT_g . The second corresponds to the temperature drop on the capacitive element, $\Delta T_{C_{th}}$. We are thus seeking the response of a heat capacitance connected in series to a heat conductance, to which is applied an external time varying temperature $\Delta T(t)$. The equation, describing the evolution of Q_{th} , the heat energy transferred to the capacitance, is given by

$$R_{th} \frac{dQ_{th}}{dt} + \frac{Q_{th}}{C_{th}} = \Delta T(t), \quad (8)$$

where $R_{th} = 1/g_{th}$ is the heat resistance.

Figure 4 displays a schematic representation of the heat propagating from a fluctuating temperature source entering at the top, flowing down the heat conductance g and accumulating in the heat capacitance at the bottom C . (For a negative change in temperature the direction of heat flow is reversed.) The vertical axis represents the temperature; as C absorbs or emits heat, it will ascend or descend. If the horizontal axis is taken to represent the position between the external contact and the channel, then the inclination of conductance element g represents the temperature gradient; this is proportional to the heat current g .

As shown in Figure 5, the electrical analogy is well known: the response of the temperature deviation $\Delta T_{C_{th}}$ to the external change ΔT in temperature is analogous to the voltage on a capacitor in an R-C circuit driven by the variation of a voltage source. In particular the channel temperature deviation corresponds to the voltage drop on the capacitor,

$$\Delta T_{C_{th}} \longleftrightarrow V_C \quad (9)$$

while the voltage source corresponds to the externally driven temperature change,

$$\Delta T \longleftrightarrow V_s \quad (10)$$

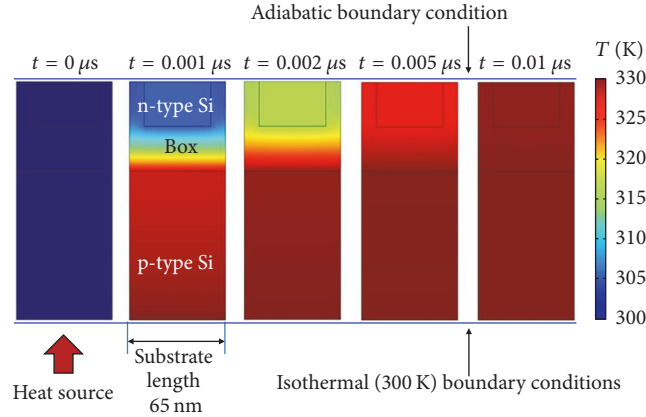


FIGURE 3: COMSOL cross section (channel plane) simulation of a 300 K to 330 K instantaneous temperature increase applied at the bottom of the SOITAM device (100 nm thick substrate and 30 nm thick BOX layer). The temperature stabilizes at the device surface after approximately 0.01 μ s.

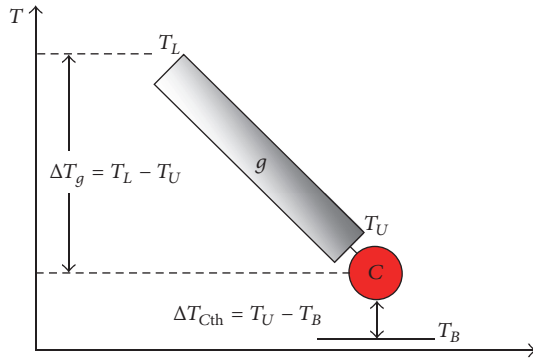


FIGURE 4: Schematic representation of the lumped model, showing a conductive element, with thermal conductance g , and a capacitive element, with heat capacity C . When T_L is perturbed above the equilibrium value, heat flows through g to C .

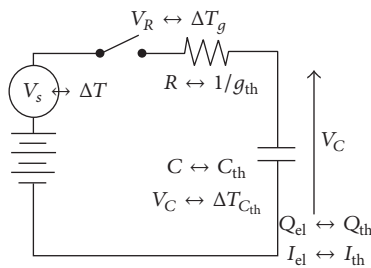


FIGURE 5: Equivalent circuit model. Equivalence mapping to the thermal problem is displayed at right.

and the voltage drop on the resistor corresponds to the temperature drop on the heat conductor,

$$\Delta T_g \longleftrightarrow V_R. \quad (11)$$

The charge accumulated by the capacitor is analogous to the heat transfer,

$$Q_{th} \longleftrightarrow Q_{el} \quad (12)$$

and the electric current describes the heat current, or energy flow,

$$I_{th} \longleftrightarrow I_{el}. \quad (13)$$

In the large signal analysis one substitutes, for $t > 0$,

$$\Delta T(t) = \Delta T_0 \quad (14)$$

into (8). This is an RC circuit connected by a switch to a DC voltage source,

$$V_{s,0} \longleftrightarrow \Delta T_0. \quad (15)$$

The switch is initially open; at time $t = 0$ the switch is closed, and the capacitor begins charging; the voltage drop across the capacitor builds and then saturates. Solving (2) for $Q_{th}(t)$ just as for the electrical circuit and using the relation

$$\Delta T_{C_{th}}(t) = \frac{Q_{th}(t)}{C_{th}} \quad (16)$$

we obtain a solution for the time-dependent response of the channel temperature $T_{Ch}(t)$ at the (upper) end of the substrate:

$$T_{Ch}(t) = T_B + \Delta T_{C_{th}}(t) = T_B + \Delta T_0 \left(1 - \exp\left(-\frac{t}{\tau}\right) \right), \quad (17)$$

where $\tau = R_{th}C_{th}$ is the characteristic decay time. The study of the large scale signal response was performed in [29]. For the small signal analysis the right hand side of (8) is given by

$$\Delta T(t) = \Delta T_0 \sin \omega t. \quad (18)$$

This describes an R-C circuit with an AC driving voltage of amplitude $V_{s,0}$, under the correspondence $V_{s,0} \leftrightarrow \Delta T_0$. In the electrical model the response, the voltage drop on the capacitor, will be sinusoidal with an amplitude $V_{C,0}$ and a phase φ . This corresponds to a sinusoidal temperature deviation of the heat capacitance

$$\Delta T_{C_{th}}(t) = \Delta T_{C,0} \sin(\omega t + \varphi). \quad (19)$$

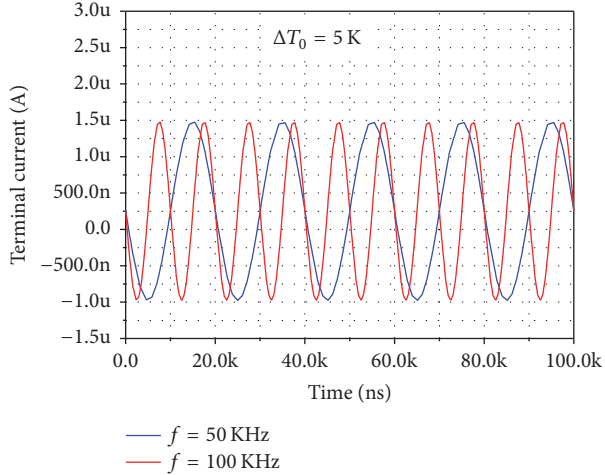


FIGURE 6: Superposition of the current curves as a function of the time for several frequencies of $f = 50$ KHz and 100 KHz. $\Delta T_0 = 5$ K. (Results obtained by the numerical simulation of the device.)

Finally the temperature time response $T_U(t)$ at the (upper) boundary end of the substrate, the location of the channel, is

$$T_U(t) = T_B + \Delta T_C(t) = T_B + \Delta T_{C,0} \sin(\omega t + \varphi), \quad (20)$$

where $\tan \varphi = -\omega R_{th} C_{th}$.

3.4. Channel Current-Temperature Phase Extraction. The small signal analysis was implemented in Comsol by setting the input temperature at the lower boundary according to

$$T(t) = T_B + \Delta T_0 \sin(\omega t), \quad (21)$$

where $T_B = 300$ K and $\Delta T_0 = 5$ K and where

$$f = \frac{\omega}{2\pi}. \quad (22)$$

The simulated current in the channel is a sinusoidal function which lagged behind the input temperature variation by a phase φ :

$$I(t) = \Delta I_0 \sin(\omega t + \varphi). \quad (23)$$

We started the simulations using low frequencies of 50 and 100 kHz, respectively, which are reasonable for thermal signal fluctuations analysis [25].

As observed in Figure 6, there is neither attenuation nor shift for such frequencies, so we decided to move to upper values, in order to calculate the expected cut-off frequency response. We pointed out that significant changes occur at frequency above 40 MHz. Though this frequency is unrealistically high for thermal fluctuations, we would like to go on with the analysis in order to test the coherence of the simulation results. An illustration of a significant shift between the temperature signal and the simulated current is observed at 500 MHz as shown in Figure 7.

The current is depicted relative to the temperature variation in Figure 7.

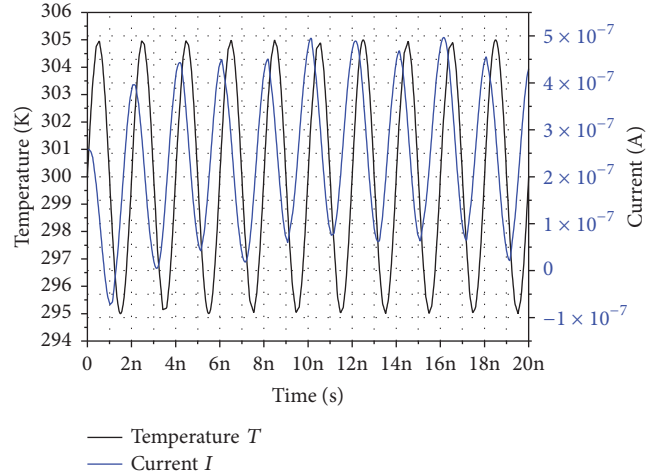


FIGURE 7: Double-axis behavior of the current and the temperature as a function time. $f = 500$ MHz and $\Delta T_0 = 5$ K.

To obtain the phase we make use of the trigonometric identity:

$$\sin \theta \sin \varphi = \frac{1}{2} (\cos(\theta - \varphi) - \cos(\theta + \varphi)). \quad (24)$$

We use this to compute the product of input temperature signal and output channel current variation (the difference between the instantaneous current $I(t)$ and the DC offset value).

$$\begin{aligned} \Delta I_0 \sin(\omega t + \varphi) \cdot \Delta T_0 \sin(\omega t) \\ = \frac{1}{2} \Delta I_0 \Delta T_0 \{ \cos(\varphi) - \cos(2\omega t + \varphi) \}. \end{aligned} \quad (25)$$

This represents a sinusoidal fluctuation of twice the input frequency having a DC value of

$$\frac{\Delta I_0 \Delta T_0}{2} \cos(\varphi). \quad (26)$$

The phase can be extracted by averaging the product in (26) over a whole number of cycles, leaving only the expression in (27). Simulations were run with Comsol at different frequencies up to 100 MHz. The phase between the channel current and the boundary temperatures was then extracted using Matlab.

The frequency dependence of the phase tangent $\tan(\varphi)$ is presented in Figure 8.

According to the low pass filter model, the phase tangent $\tan \varphi$ depends on the frequency f as

$$-\tan \varphi(f) = 2\pi f R_{th} C_{th}. \quad (27)$$

Equation (25) predicts a linear curve, as seen in Figure 8 for $f < 100$ MHz, using the graph we can extract a value of thermal time constant $R_{th} C_{th}$, from the slope of a linear regression curve (Figure 8); this renders a value of 2.1 ns.

3.5. Current Sensitivity. In order to simulate the current sensitivity of the silicon-based sensor in the RF frequency

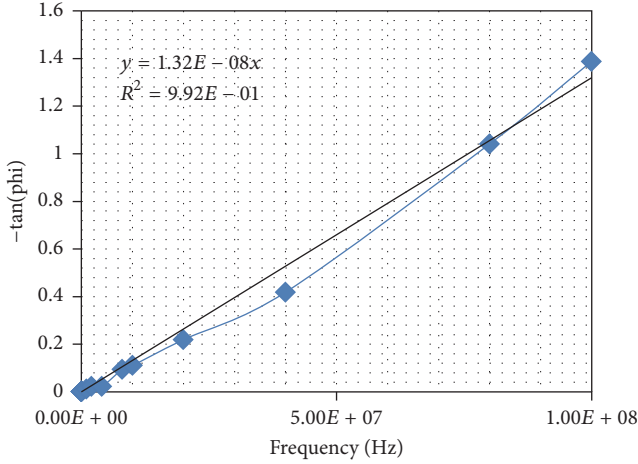


FIGURE 8: Graph representing the variation of phase tangent $\tan(\varphi)$ as a function of the frequency.

domain, several tests were done when varying different parameters such as frequency and temperature amplitude. Following is a comparison of the results. Figure 9 shows the simulated response of the device when the temperature amplitude ΔT_0 is fixed, and the frequency is varied. The input temperature at the lower boundary is given by (22), where $T_B = 300$ K, $\Delta T_0 = 5$ K, and where this time

$$f = \frac{\omega}{2\pi} = 500 \text{ MHz and } 1 \text{ GHz, respectively.} \quad (28)$$

We note decreasing of the current amplitude with the frequency as expected by the low pass filter RC model.

In Figure 10, the amplitude of the temperature variation is now varied from 1 K to 4 K, and the frequency remains fixed at 500 MHz. This time, the corresponding input temperature is given by the equation

$$T = 300 + \Delta T_0 \sin(2\pi ft), \quad (29)$$

where $\Delta T_0 = 1$ K, 2 K, 3 K, and 4 K, respectively, and $f = 500$ MHz.

As shown in Figure 10, the current response is linear with the temperature and the obtained sensitivity (CST) has an order of magnitude in $\mu\text{A/K}$ which is reasonable to be detected. Note that other thermal detectors like thermocouples or CMOS sensors [24–28] have a voltage response to temperature. Thermocouples, for instance, have a typical voltage response of $50 \mu\text{V/K}$ and MOSFET sensor is reported to have 1.6 mV/K [25]. Consequently, the direct comparison of our results with those of other reported devices is not straightforward.

3.6. Theoretical Transfer Function and Time Constant Extraction. We are interested to check if the current sensitivity to temperature (CST) of the sensor ($\mu\text{A/K}$) behaves with frequency like a theoretical transfer function $H(\omega)$, of an RC circuit, a low pass filter, given by

$$|H(\omega)| = \frac{1}{\sqrt{1 + (\omega RC)^2}}. \quad (30)$$

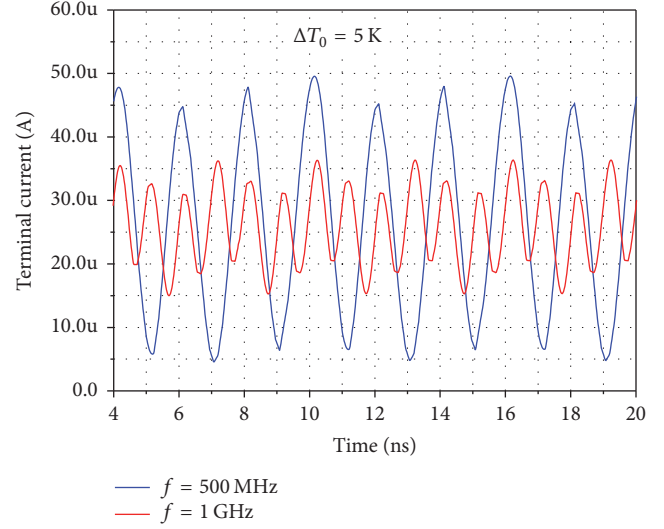


FIGURE 9: Superposition of the current curves as a function of the time for several frequencies of $f = 500$ MHz and 1 GHz. $\Delta T_0 = 5$ K. (Results obtained by the numerical simulation of the device.)

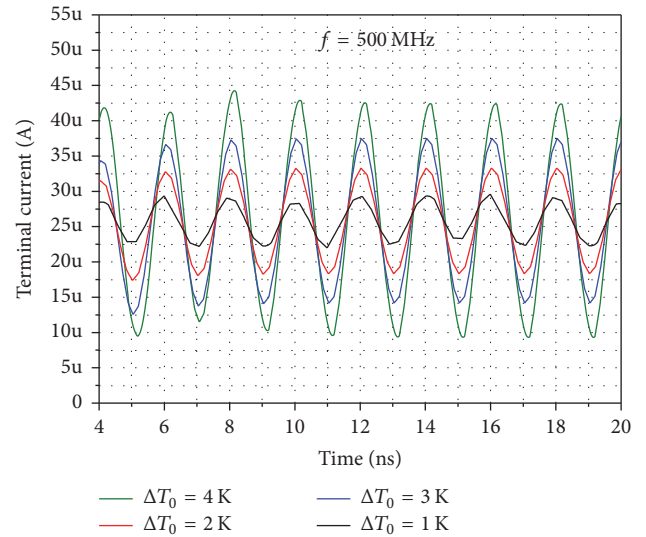


FIGURE 10: Superposition of the current curves as a function of the time for frequency $f = 500$ MHz, $\Delta T_0 = 1$ K, 2 K, 3 K, and 4 K. (Results obtained by the numerical simulation of the device.)

To this end we consider the response function obtained from the ratio of the amplitudes of the output current variation to the input temperature variation, $\Delta I_0(f)/\Delta T_0$.

The result is presented in the graph (Figure 11) and well described by (31) as depicted in the inset.

The graph can be of course exploited to extract the (thermal) RC constant from the cut-off frequency f_c defined by $H(f_c) = 1/\sqrt{2} = 0.707$ point; that is, $f_c = 90$ MHz. This gives a value of

$$R_{\text{th}}C_{\text{th}} = \frac{1}{2\pi f_c} \cong 1.8 \text{ ns} \quad (31)$$

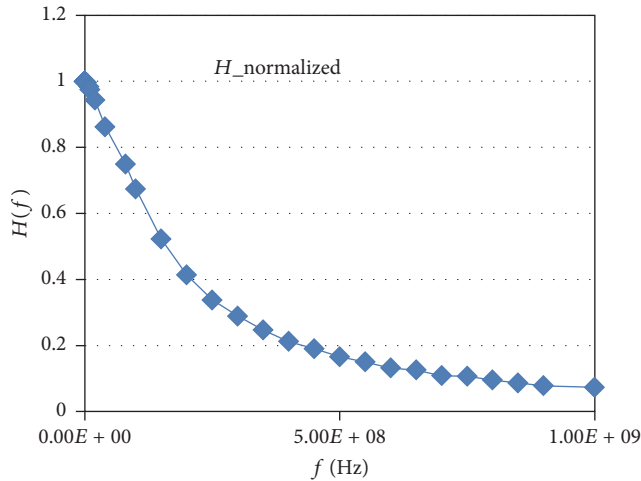


FIGURE 11: Normalized current sensitivity to temperature as function of frequency.

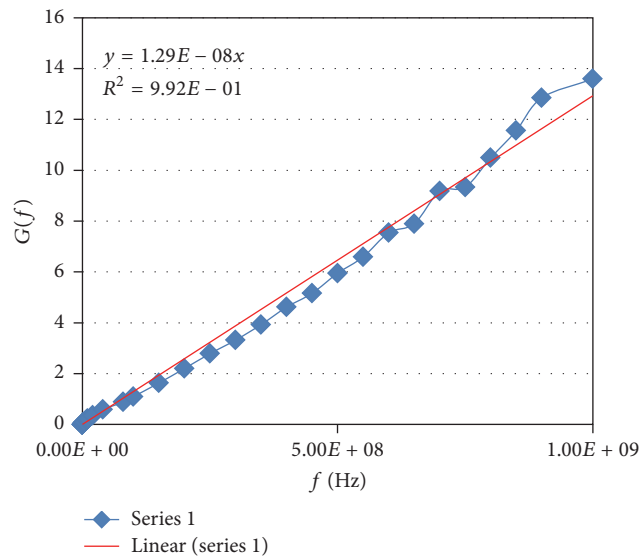


FIGURE 12: Distribution of the response function as a function of the frequency.

which is consistent with the value we deduced above from the phase. As for the phase, a more precise value is obtained by a linear fit, this time using the linearized function G defined by

$$G(\omega) \equiv \sqrt{\frac{1}{H(\omega)^2} - 1} = \omega R_{th} C_{th} = 2\pi f R_{th} C_{th}. \quad (32)$$

The linear dependence is confirmed in Figure 12. Calculating the linear fit gives the value $R_{th} C_{th}$ of 2 ns, again consistent with the value derived from the cut-off frequency and from the phase-frequency dependence.

Since we are dealing with a nanoscale device, due to its small dimensions, thermal equilibration is extremely rapid. The large signal simulation demonstrates that response times are very small (as seen in Figure 3).

Although we are aware that a GHz frequency for thermal signal is not physically relevant, we would like to show the frequency response of the simulated device in order to ensure that the simulation predicts an expected “low pass” behavior.

Indeed, a high cut-off frequency (90 MHz) is obtained which is consistent with the small dimensions of the device but as mentioned such high frequency is irrelevant for practical purposes.

Similarly the small signal simulation demonstrates that the thermal phase lag is insignificant up to frequencies of 500 MHz or 1 GHz, which as the reviewer justly points out are not encountered in practice. Thus, though in principle the system acts as a low pass filter, the simulation demonstrates that attenuation is not encountered until frequencies are so high, as to be irrelevant for practical purposes.

4. Conclusions

When dealing with new type of sensor, it was important to establish its accuracy and responsivity not only for large signals, but mainly for more small ones. We have shown that a small signal analysis of the electrical current response to temperature can be coherently modeled by an RC equivalent low pass filter model in the RF frequency domain. Due to the nanoscale dimensions of our simulated device, the time response was found as low as 2 ns and the current sensitivity is in the $\mu A/K$ order of magnitude. Those encouraging results should path the way for such kind of nanoscale silicon-based device to be integrated in microelectronics circuit as an efficient thermal sensor of realistic thermal fluctuation in the kHz range frequency.

Conflicts of Interest

The authors declare that there are no conflicts of interest regarding the publication of this paper.

References

- [1] V. R. Almeida, C. A. Barrios, R. R. Panepucci, and M. Lipson, “All-optical control of light on a silicon chip,” *Nature*, vol. 431, no. 7012, pp. 1081–1084, 2004.
- [2] J. Mason, “Development of on-chip optical interconnects for future multi-core processors,” *Smart Data Collective*, vol. 29, 2007, <http://www.smartdatacollective.com/jackmason/22794/development-chip-optical-interconnects-future>.
- [3] N. Savage, “Linking chips with light,” *IEEE Spectrum*, vol. 53, no. 2, pp. 11–12, 2016, <http://spectrum.ieee.org/semiconductors/optoelectronics/linking-chips-with-light>.
- [4] A. Karsenty, A. Sa’ar, N. Ben-Yosef, and J. Shappir, “Enhanced electroluminescence in silicon-on-insulator metal-oxide-semiconductor transistors with thin silicon layer,” *Applied Physics Letters*, vol. 82, no. 26, pp. 4830–4832, 2003.
- [5] L. W. Snyman, M. du Plessis, E. Seevinck, and H. Aharoni, “An efficient low voltage, high frequency silicon CMOS light emitting device and electro-optical interface,” *IEEE Electron Device Letters*, vol. 20, no. 12, pp. 614–617, 1999.
- [6] M. E. Castagna, S. Coffa, M. Monaco et al., “High efficiency light emitting devices in silicon,” *Materials Science and Engineering: B*, vol. 105, no. 1–3, pp. 83–90, 2003.

- [7] Z. Zalevsky, "Integrated micro- and nanophotonic dynamic devices: a review," *Journal of Nanophotonics*, vol. 1, no. 1, Article ID 012504, 2007.
- [8] D. Abraham, Z. Zalevsky, A. Chelly, and J. Shappir, "Fabrication of vertically positioned silicon on insulator photo-activated modulator," *Photonics and Nanostructures—Fundamentals and Applications*, vol. 7, no. 4, pp. 190–197, 2009.
- [9] A. Liu, R. Jones, L. Liao et al., "A high-speed silicon optical modulator based on a metal–oxide–semiconductor capacitor," *Nature*, vol. 427, no. 6975, pp. 615–618, 2004.
- [10] Q. Xu, B. Schmidt, S. Pradhan, and M. Lipson, "Micrometre-scale silicon electro-optic modulator," *Nature*, vol. 435, no. 7040, pp. 325–327, 2005.
- [11] D. Abraham, Z. Zalevsky, A. Chelly, J. Shappir, and M. Rosenbluh, "Silicon on insulator photo-activated modulator," *Microelectronics Journal*, vol. 39, no. 12, pp. 1429–1432, 2008.
- [12] A. Zev, A. Chelly, A. Karsenty, and Z. Zalevsky, "Development, simulation and characterization of nanoscale silicon on insulator photo-activated modulator (SOIPAM) hybrid device," in *Proceedings of the International Conference on Optical MEMS and Nanophotonics (OMN '15)*, pp. 1–2, IEEE, Jerusalem, Israel, August 2015.
- [13] A. Zev, A. Karsenty, A. Chelly, and Z. Zalevsky, "Nanoscale silicon-on-insulator photo-activated modulator building block for optical communication," *IEEE Photonics Technology Letters*, vol. 28, no. 5, pp. 569–572, 2016.
- [14] S. Mias, J. Sudor, and H. Camon, "PNIPAM: a thermo-activated nano-material for use in optical devices," *Microsystem Technologies*, vol. 14, no. 4–5, pp. 691–695, 2008.
- [15] M. Aleksandrova, N. Nikolov, and I. Pandiev, "Thermo-stimulation of charges by peltier element for trap analysis in polymer layers," *International Journal of Polymer Analysis and Characterization*, vol. 16, no. 4, pp. 221–227, 2011.
- [16] J. Ferreira, Benefits of Silicon-Based Temperature Sensors, Metrology, Quality Digest, December 2012.
- [17] M. Mansoor, I. Haneef, S. Akhtar, A. De Luca, and F. Udrea, "Silicon diode temperature sensors—a review of applications," *Sensors and Actuators A: Physical*, vol. 232, pp. 63–74, 2015.
- [18] I. Tobehn, A. Steinke, A. Albrecht, H. Hansch, M. Kunze, and T. Ortlepp, "Silicon based temperature sensors with extended temperature range and simple one-point calibration," in *Proceedings of the The Sixth International Conference on Sensor Device Technologies and Applications*, pp. 50–53, 2015.
- [19] F. Fruett, G. Wang, and G. C. M. Meijer, "Piezojunction effect in NPN and PNP vertical transistors and its influence on silicon temperature sensors," *Sensors and Actuators*, vol. 85, no. 1, pp. 70–74, 2000.
- [20] S. Maeng, P. Guha, F. Udrea et al., "SOI CMOS-based smart gas sensor system for ubiquitous sensor networks," *ETRI Journal*, vol. 30, no. 4, pp. 516–525, 2008.
- [21] P. K. Guha, S. Z. Ali, C. C. C. Lee et al., "Novel design and characterisation of SOI CMOS micro-hotplates for high temperature gas sensors," *Sensors and Actuators B: Chemical*, vol. 127, no. 1, pp. 260–266, 2007.
- [22] S. Santra, F. Udrea, P. K. Guha, S. Z. Ali, and I. Haneef, "Ultra-high temperature (>300°C) suspended thermodiode in SOI CMOS technology," *Microelectronics Journal*, vol. 41, no. 9, pp. 540–546, 2010.
- [23] F. Udrea and J. Gardner, "SOI CMOS gas sensors," in *Proceedings of the IEEE SENSORS 2002*, pp. 1379–1384, Orlando, FL, USA.
- [24] M. A. Huque, L. M. Tolbert, B. J. Blalock, and S. K. Islam, "A high-temperature, high-voltage SOI gate driver IC with high output current and on-chip low-power temperature sensor," in *Proceedings of the 42nd International Symposium on Microelectronics (IMAPS '09)*, pp. 220–227, November 2009.
- [25] F. Reverter, D. Gomez, and J. Altet, "On-chip MOSFET temperature sensor for electrical characterization of RF circuits," *IEEE Sensors Journal*, vol. 13, no. 9, pp. 3343–3344, 2013.
- [26] F. Reverter, X. Perpiñà, E. Barajas et al., "MOSFET dynamic thermal sensor for IC testing applications," *Sensors and Actuators A: Physical*, 2015.
- [27] F. Reverter, X. Perpiñà, J. León, M. Vellvehi, X. Jordà, and J. Altet, "Characterization of MOSFET temperature sensors for on-chip dynamic thermal measurements," *Procedia Engineering*, vol. 120, pp. 836–839, 2015.
- [28] C. Zhao, CMOS on-chip temperature sensors for power management (2014). Graduate Theses and Dissertations. Paper 13649.
- [29] Y. Mandelbaum, A. Zev, A. Chelly, Z. Zalevsky, and A. Karsenty, "Study of the Photo- and Thermoactivation Mechanisms in Nanoscale SOI Modulator," *Journal of Sensors*, vol. 2017, Article ID 9581976, 11 pages, 2017.



Hindawi

Submit your manuscripts at
<https://www.hindawi.com>

